Towards fiber coupled cavity quantum electrodynamics

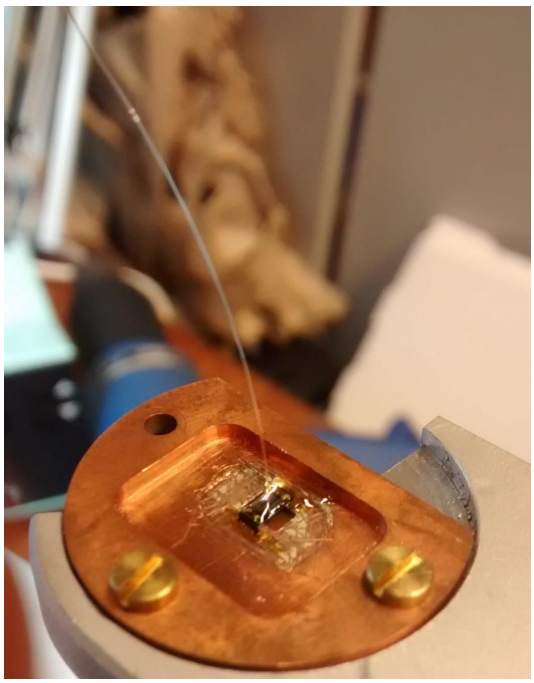

THESIS

submitted in partial fulfillment of the
requirements for the degree of

MASTER OF SCIENCE
in
PHYSICS

Author :	BSc. Vincent P. Post
Student ID :	1137344
Supervisors :	Prof.dr. Dirk Bouwmeester
	Dr. Wolfgang Löffler
	MSc. Henk Snijders
2^{nd} corrector :	Prof.dr. Michel A.G.J. Orrit

Leiden, The Netherlands, September 22, 2016

Towards fiber coupled cavity quantum electrodynamics

BSc. Vincent P. Post

Huygens-Kamerlingh Onnes Laboratory, Leiden University
P.O. Box 9500, 2300 RA Leiden, The Netherlands

September 22, 2016

Abstract

A cavity quantum electrodynamics system consisting of quantum dots in a micropillar cavity may form an essential building block for the creation of a quantum network. Current systems do not allow for the scaling, in a simple manner, to a large network. Therefore, we introduce a scalable approach by coupling a micropillar cavity to single-mode fibers. The steps taken to achieve the fiber coupling are explained and the first tests for researching a fiber coupled cavity quantum electrodynamics system are shown. The first tests show that full input-output fiber based polarization control of a micropillar cavity at 3.5 K is possible which is important for a photon polarization based quantum network. Several experimental challenges are shown and discussed. Despite the experimental challenges, the first tests may pave the way for a more scalable approach for building a large-scale quantum network.

Contents

Chapter 1

Introduction

Quantum phenomena are one of the most active research areas today, this is evidenced by the 1 billion euro Europe based quantum technologies flagship announced recently [1]. The flagship rests on the fact that some quantum technologies are already starting to be commercially exploited and that our ability to manipulate quantum effects in customised systems and materials is improving. An application of quantum phenomena may be the building of a quantum network that forms the backbone of distributed quantum computing architectures and quantum communication [2]. Such a quantum network consists of nodes that are capable of sending, receiving, storing and releasing photonic quantum information. The nodes are linked by quantum channels that transport quantum states from node to node with high fidelity and can distribute entanglement over all the nodes. The nodes require a non-linear system for the quantum network to work. An example of a possible quantum network scheme is an atom or an artificial atom, a so called quantum dot (QD), placed inside a cavity that functions as a node by encoding the quantum information in the spin of an electron situated in the QD [3]. The quantum information is transferred by means of the polarization of the photon, in the quantum channels. The quantum network may not lose its quantum information in a long time-span, therefore a long coherence time is needed, and the quantum network needs to exhibit high fidelity. Both requirement are satisfied by encoding the quantum information in the polarization of the photon and in the electron spin of the QD (under specific circumstances).

For the creation of a large quantum network, integration of the atom or QD into the solid state is a promising path to take. Integration into the solid state is simpler with QDs than with atoms. Therefore, our design is focused on QDs located in a micropillar cavity [4]. Even though solid state integration allows for less optical elements needed to let the system function as a node, scaling to

multiple connected nodes remains an experimental challenge. A possible way to remove almost all optical elements is by permanently coupling optical fibers on the in- and output of each node in the network. The requirements for the fibers are that they are single-mode fibers such that the polarization and phase information is not lost. Of course, the fibers need to be coupled with a high coupling efficiency with the node to minimize losses.

This cavity quantum electrodynamics (CQED) system of QDs in a micropillar cavity is not only important for a quantum network, it may also function as a generator of non-classical states of light, such as a high-fidelity source of single photons [5] or a source of bunched photons [6].

We will show in this thesis the first tests on the coupling of a single QD-cavity system to optical fibers. The fiber coupling is built on the group's acquired experience with coupling fibers to CQED devices such as a ring resonator [7] or an older design on QDs in a micropillar cavity [8]. Before the first tests are shown, a simple theory behind a QD coupled to an optical cavity is shown (chapter 2.1). Next the design of our CQED device is shown and discussed (chapter 2.2). Then the transmission and reflection of a micropillar cavity from transfer matrix simulation are examined (chapter 2.3) and at the end of chapter 2 the requirements to see the influence of our QDs are listed (chapter 2.4). Chapter 3 gives a theoretical calculation of the coupling efficiency at the in- and output of a micropillar cavity with two 780HP single-mode fibers. In chapter 4 we will explain how the coupling of fibers onto the micropillar cavity is achieved. Chapter 5 presents and discusses the first tests of cooling down our fiber coupled device to cryogenic temperatures. Cryogenic temperatures are needed for preserving the electrons spin coherence in the QDs. In the end, in chapter 6, future improvements are discussed.

Chapter 2

Theory

In this chapter we introduce the theory behind a quantum dot in an optical cavity. The theory uses a simple picture of a quantum dot described by a two-level system. Next we discuss the device that allows us to research cavity quantum electrodynamics. Finally, it is explained why cryogenic temperatures are needed and why a voltage needs to be applied to the device.

2.1 Two-level system in a cavity

A quantum dot (QD) described in a simple picture can be seen as a two-level system. The two-level system is inserted into an optical cavity, so that one obtains strong and deterministic photon-QD interaction. To sketch a simple naive quantitative picture of how to achieve deterministic photon-QD interaction we compare the interaction of the light with a QD in or out of an optical cavity. For the QD out of the cavity to have deterministic photon-QD interaction, one needs the absorption cross section of the QD (on resonance, σ_{abs}) to be larger than the area of the light beam [9]:

$$\underbrace{\frac{3\lambda^2}{2\pi}}_{\sigma_{abs}} >> \underbrace{\frac{\pi}{4}w_0^2}_{\text{beam area}} \tag{2.1}$$

Here, λ is the resonance wavelength of the QD and w_0 is the beam waist. If we fill in typical values of our device, $\lambda = 950$ nm and $w_0 = 2$ µm we obtain $0.43 \ggg \pi$, i.e., deterministic photon-QD interaction is not possible. When the

QD is inserted into the cavity the equation changes to:

$$\underbrace{\frac{3\lambda^2}{2\pi}}_{\sigma_{abs}} \times \underbrace{\frac{\mathcal{F}}{\pi}}_{\text{bounces}} >> \underbrace{\frac{\pi}{4} w_0^2}_{\text{beam area}} \tag{2.2}$$

Here, $\mathcal{F}$ is the finesse of the cavity. If we fill in the typical value of our cavity finesse $\mathcal{F} = 1000$ we obtain $137 \gg \pi$. Therefore, deterministic photon-QD interaction is possible.

This naive simple picture in equation 2.2 can be rewritten in terms of the key parameters that describe a cavity containing a two-level system [9]:

- The QD-cavity coupling constant, g. Defined as:

$$g = \frac{\mu_{ge} E}{\hbar} = \sqrt{\frac{\mu_{ge}^2 \omega_{cav}}{2\epsilon_0 \hbar V}} u(\vec{x}) \tag{2.3}$$

  In this equation E is electric field of a single photon entering the cavity, μ_{ge} the electric dipole matrix element that links the atomic transition between the ground and excited state, $\hbar$ is the reduced Planck constant, ϵ_0 is the permittivity of free space, ω_{cav} is the cavity angular frequency and the mode volume $V = \int u^2(\vec{x}) d^3x$ expressed as an integral over the dimensionless electric mode function $u(\vec{x})$ of the resonator, normalized to 1 at the field maximum.

- The cavity field decay rate, κ. It is defined as:

$$\kappa = \frac{\pi c}{2L\mathcal{F}} \tag{2.4}$$

  Here, c is the speed of light, L the resonator length and $\mathcal{F}$ the finesse of the cavity.

- The radiative decay rate of the QD in vacuum, γ.

$$\gamma = \frac{\mu_{ge}^2 \omega_{cav}^3}{6\pi\epsilon_0 \hbar c^3} \tag{2.5}$$

The simple picture already shows most of the relevant experimental parameters. For example, the mode volume V in Eq. 2.3 shows that a cavity with a small mode volume is important for increasing the coupling between the QD

and cavity by increasing g. The smaller mode volume also leads to the so-called Purcell enhancement of the spontaneous emission rate of the QD [3]:

$$F_P = \frac{3Q}{4\pi^2 V}\left(\frac{\lambda}{n}\right)^3 \tag{2.6}$$

Here, Q is the quality factor of the cavity defined by $Q = \frac{\omega}{\Delta\omega}$ and n the refractive index of the active region of the cavity. In equation 2.6 the two-level system transition is resonant with the cavity, the cavity only sustains a single mode and the two-level system (actually just a dipole) is oriented along the field direction.

With the key parameters: g, κ and γ, Equation 2.2 can be rewritten into [9]:

$$C = \frac{g^2}{2\kappa\gamma} \gg 1 \tag{2.7}$$

Here, C denotes the single-atom cooperativity parameter. A typical value for the cooperativity of our device [6] is $C = 1.7$. Even though we obtain deterministic photon-QD interaction two situations can arise [9] depending on the values of g, κ and γ. (i) The strong coupling regime: $g \gg (\gamma, \kappa)$ the QD-photon coupling is faster than all irreversible processes, such that the reversible process of vacuum-Rabi osccilations can occur. (ii) The Purcell regime: $\kappa \gg g \gg \gamma$ a photon that is emitted into the cavity mode is lost from the resonator before it can be reabsorbed by the QD, even though the density of photonic modes is considerably changed by the presence of the cavity. Therefore, the dynamics of the QD-cavity is different from the QD in free space. This is the regime our device is in.

The simple picture can be extended to obtain a basic understanding of the dynamics of a lossless coupled QD-cavity system. This is achieved by describing it as a canonical Jaynes-Cummins model [10]. The basic physical situation is sketched in Figure 2.1(a), where also the corresponding parameters are shown. The cavity only supports a single optical mode which is at a frequency ω_{cav}. This frequency is close to (or in) resonance with the QD transition from the excited($|e\rangle$) to the ground state($|g\rangle$) at a frequency ω_{QD}. For the corresponding Jaynes-Cummings Hamiltonian we assume that the QD is in the ground state and no photons are in the cavity. Also the QD exchanges energy with the cavity at a rate $2g$. The Jaynes-Cummings Hamiltonian written in the interaction picture with time dependent operators and with the rotating wave approximation is given by:

$$H_{JC} = \underbrace{\hbar\omega_{QD}\sigma_{ge}^{\dagger}\sigma_{ge}}_{\text{bare QD}} + \underbrace{\hbar\omega_c a^{\dagger}a}_{\text{empty cavity}} + \underbrace{\hbar g(\sigma_{ge}^{\dagger}a + \sigma_{ge}a^{\dagger})}_{\text{dipole coupling}} \tag{2.8}$$

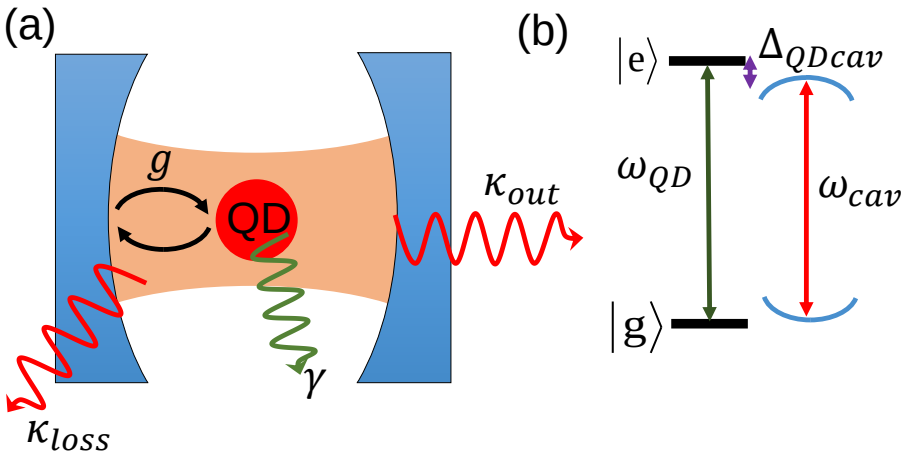

Figure 2.1: *(a) Cartoon of a quantum dot (QD), visualized as a two-level system, in a cavity. The coupling between the QD and cavity is given by a constant g. The cavity field decay rate is $\kappa = \kappa_{out} + \kappa_{loss}$. Where κ_{out} is what will be collected in transmission and κ_{loss} is lost from the cavity and therefore is not collected. The decay rate of the QD is γ. (b) The QD and cavity energy level scheme. The transition frequency between the ground state $|g\rangle$ and excited state $|e\rangle$ is ω_{QD}. The cavity resonance frequency is ω_{cav}. The QD and cavity are detuned by $\Delta_{QDcav} = \omega_{QD} - \omega_{cav}$.*

Here $\sigma_{ge} = |g\rangle\langle e|$ and $\sigma_{ge}^{\dagger} = |e\rangle\langle g|$ are the QD lowering and raising operators, and a and $a^{\dagger}$ are the annihilation and creation operators of a photon in the cavity mode, respectively.

The Jaynes-Cummings Hamiltonian explains a number of CQED phenomena, such as: dressed states and avoided crossings.

2.2 Design CQED device

Our CQED device (see the thesis of Morten Bakker [4] for more details) is shown in Fig. 2.2. The device is mounted on a copper holder with the contacts bonded onto a chip carrier, which is connected to electrical pins, see Fig. 2.2.a. Fig. 2.2.b. shows a microscope image of the device on which we see multiple etched areas in the shape of nuclear signs and a p- and n-contact area to bond wires on. Each nuclear sign has in the middle a micropillar cavity, a total of 42, each with a slightly different radius and ellipticity of the micropillar. The mean micropillar size is roughly 15 μm in radius and is circular. Each micropillar therefore has a different mode volume and therefore a different coupling of the QD to the cavity, see Eq. 2.3. The high number of micropillars on a device increases the chance that a QD is located exactly in the center of the cavity, where the QD-

cavity coupling is best. Also, the higher number of micropillars increases the chance of having a micropillar cavity that has a polarization degenerate fundamental mode, which is important for quantum information applications [3]. Our devices are optimized to be nearly polarization degenerate, further, there is a possibility to tune them to degeneracy by using laser induced surface defects [11].

What is shown in Fig. 2.2.c is a scanning electron microscope image of a micropillar cavity and the trenches around it. The nuclear sign is created by etching away multiple layers of the device. This is needed for the wet-chemical oxidation of an aluminium arsenide (AlAs) layer to create a so-called tapered oxide aperture. In Fig. 2.2.d a schematic drawing of the micropillar cavity is shown, in which the oxide aperture is shown slightly above the QDs. The schematic drawing in Fig. 2.2.e shows a region outside of the micropillar area where no oxide aperture is visible. It will be referred to as a Fabry-Pérot cavity.

The micropillar consists of two distributed Bragg reflectors (DBR) which create longitudinal mode confinement, the cavity. The top DBR is a 26 pair of $\lambda_{\text{vac}}/(4n)$ gallium arsenide (GaAs) and 90 % aluminium 10 % gallium arsenide ($Al_{0.9}Ga_{0.1}As$) layers, while the bottom DBR has 13 alternating layers of GaAs, AlAs and then 16 alternating layers of GaAs, $Al_{0.9}Ga_{0.1}As$. The 13 layers are the first layers on top of the GaAs substrate. λ_{vac} is the wavelength in vacuum, n is the refractive index of the corresponding layer. Ideally the thickness is $\lambda_{\text{vac}}/(4n)$ for every light wave coming in, but the thickness is not changeable. Therefore, the DBRs are created with a specific design wavelength in mind. The design wavelength is chosen as 955 nm which is close to a peak in the photoluminescence spectrum of the QDs between $900 - 980$ nm [4]. The top DBR contains a 330 nm thick p-doped GaAs contact layer, carbon doped. The bottom DBR contains a 463.7 nm thick n-doped GaAs contact layer, silicon doped. Due to the doped layers in the top and bottom DBR the InAs / GaAs self-assembled lens-shaped QDs in the cavity are embedded in a P-I-N junction, enabling charge and energy control through the quantum-confined Stark effect [12]. For charge control, the QDs are separated by a 35 nm thick GaAs tunnel barrier from the n-doped contact layer.

The approximately $5\lambda_{\text{vac}}$ micropillar cavity also contains a tapered oxide aperture created by the wet chemical oxidation of a 10 nm thick AlAs layer which is embedded between a 95 nm thick $Al_{0.83}Ga_{0.17}As$ layers and a 66 nm thick $Al_{0.75}Ga_{0.25}As$ layer. The aperture enables an intra-cavity lens for transverse mode confinement. Transverse mode confinement enables small cavity mode volumes from which a better coupling between QD and cavity is obtained, see Eq. 2.3, and a Purcell enhancement, see Eq. 2.6. The transverse mode confinement give rise to Hermite-Gaussian modes [13], which are split

by approximately 1 nm. Because the Fabry-Pérot cavity does not contain an oxide aperture no Hermite-Gaussian higher order modes that are split approximately 1 nm apart are obtained. In the absence of transverse mode confinement ("Fabry-Pérot cavity"), the coupling between light and the QD is strongly reduced.

The three 'bridges' remaining in Fig. 2.2.c allow for the charges to flow to the micropillars p-contact. In Fig. 2.2.b large p- and n metal contacts are seen onto which wires can be bonded for applying a voltage to the device. For the p-doped layer it consists of Ti-Pt-Au (from bottom to the top layer visible) and for the n-doped layer it consists of Ni-AuGe-Ni-Au. By usage of rapid thermal annealing ohmic contacts are ensured. The created contacts are roughly 1.6 mm in length and 0.5 mm wide.

The actual micropillars and Fabry-Pérots are only 9.15 μm thick and are placed on top of approximately a 700 μm thick GaAs substrate. The thick substrate may significantly alter the transmission and reflection of the micropillar and Fabry-Pérot cavities. Therefore, we will show from transfer matrix simulations, in which absorption is neglected, the influence of a substrate with a specific thickness on the transmission/reflection from the micropillar cavity.

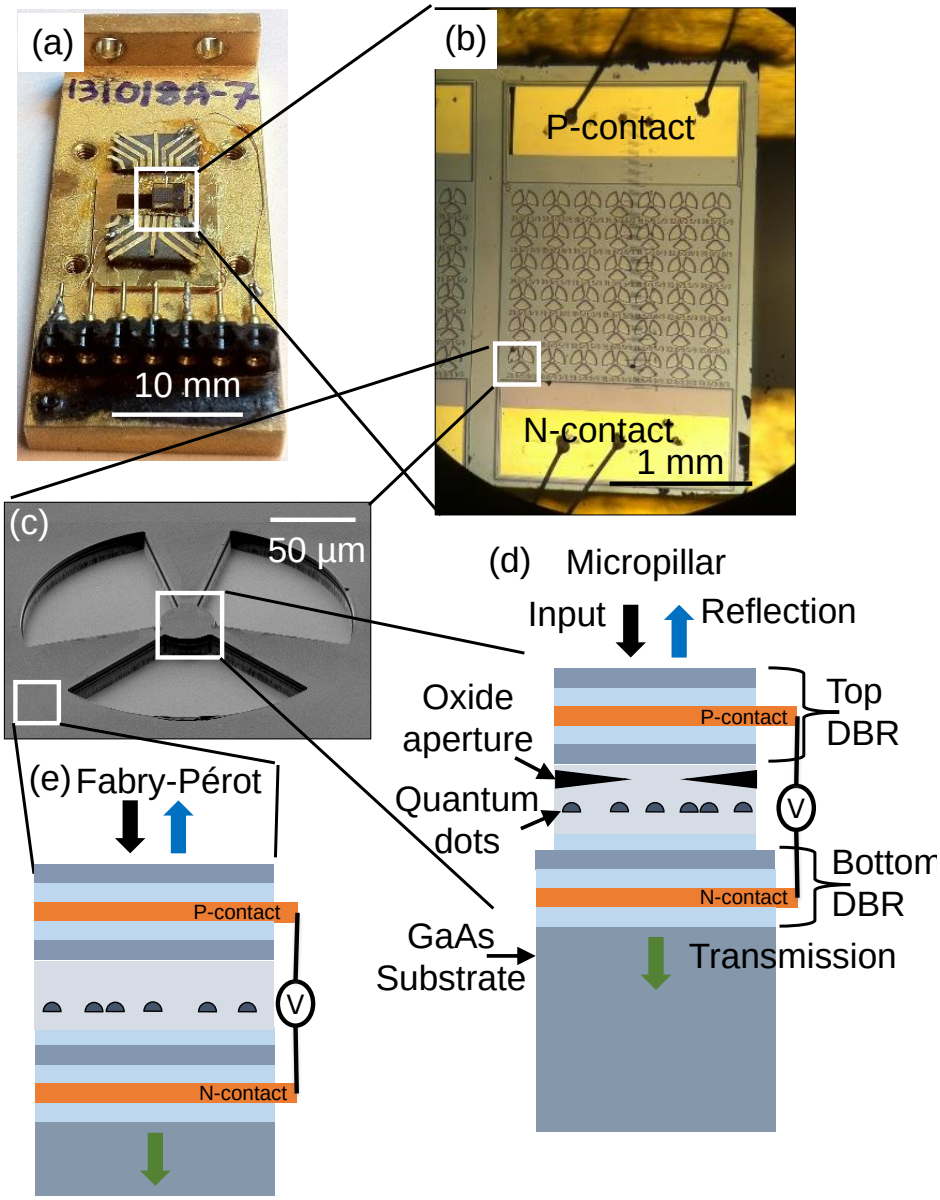

Figure 2.2: *Our device used for cavity quantum electrodynamics research. (a) The device mounted on a copper holder. (b) Optical microscope image of the device on which we see 42 micropillar cavities. Each micropillar cavity is located approximately in the center of a nuclear sign with a predefined size. (c) SEM image of one nuclear sign with a micropillar cavity in the middle. (d) Schematic drawing of the micropillar cavity which is grown on a gallium arsenide (GaAs) substrate. (e) Schematic drawing of a Fabry-Pérot cavity, differing from the micropillar cavity due to the absence of an oxide aperture.*

2.3 Transfer matrix simulation of our micropillar cavity

The transfer matrix method calculates a corresponding matrix for every layer including the acquired phase in the layer and creates a complete matrix for the device. The complete matrix can be used to calculate the total effect of the device on the transmitted intensity and reflected intensity from the device [14]. Transfer matrix methods cannot take into account transverse confinement, the methods simulate infinite wide layers, therefore it is not possible to simulate the effect of the oxide aperture onto the light. Because of this the simulations shown are of the Fabry-Pérot cavity, see Fig. 2.2.e.

The simulation of the transmitted intensity (referred to as transmission) and reflected intensity (referred to as reflection) for the Fabry-Pérot cavity without the substrate is shown in Fig. 2.3. The transmisison and reflection are both shown as a fraction of the total power transmitted. Figure 2.3 shows a simulation for light incident at normal incidence. Also, the layers in the simulation have the refractive indice values at room temperature which will change when the device is cooled down to cryogenic temperatures, but it is expected that no significant change will be seen in the transmission and reflection because the ratio of the refractive indices will roughly remain the same. Also, the materials length will change during cool down but because the materials have a low thermal shrinkage making this effect negligible. Cryogenic temperatures are needed for preserving electronic coherence in the QDs, see Section 2.4

The spectra are shown in a large wavelength band ($830 - 1070$ nm) but the interesting result is in the middle of the so-called 'stopband'($910 - 1000$ nm), where a peak in the transmission is seen. The wavelength corresponding to the peak in transmission, referred to as the cavity mode, is close to the design wavelength, see Section 2.2. The simulated cavity mode is narrow, it has a FWHM of approximately 0.01 nm which gives a high Q value, $Q = \frac{\omega}{\Delta\omega} \approx 100\,000$. Also, it has a peak transmission value of 0.56. The figure also shows that on either side of the stopband the reflectivity drops of in an oscillating fashion, this is typical for DBR microcavities.

The simulation for the micropillar with 708 μm substrate is shown in Fig. 2.4. We observe now very fast oscillations for regions with nonzero transmission and more important the cavity mode transmission is decreased and split into two peaks. The decrease and split of the cavity mode is actually only observed for specific values of the substrate thickness, this is due to small thickness variations that lead to quasi-incoherent reflections at this layer thereby removing pronounced interference effects. For example simulations of a 700 μm substrate show that the cavity mode is approximately the same as seen in Figure. 2.3.

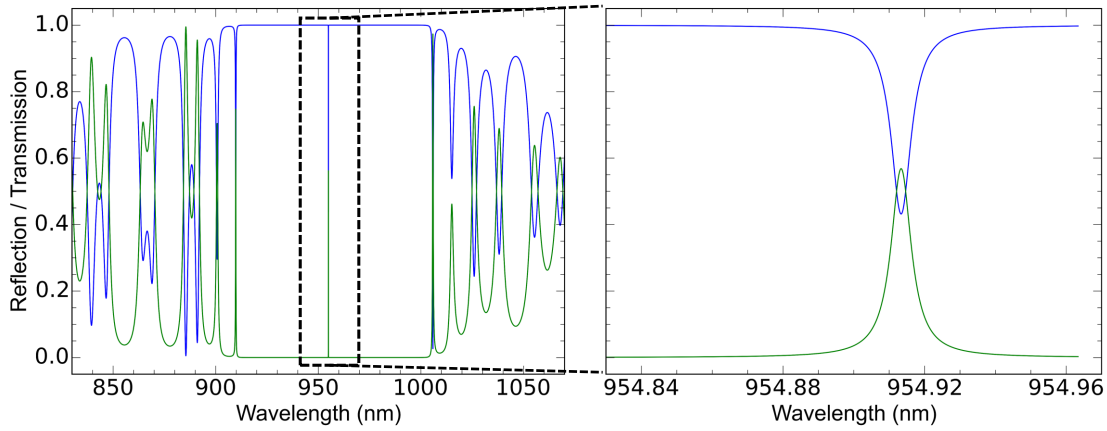

Figure 2.3: *Transmission (green line) and reflection (blue line) spectrum of normal-incident light. Both transmisison and reflection are shown as a fraction of the total power transmitted. The spectra are obtained from a transfer matrix simulation of our* 9.15 μm *thick Fabry-Pérot cavity, simulated at room temperature and for light incident from air and transmitted into air. The left panel shows an overview spectrum and the right panel shows the cavity mode spectral region.*

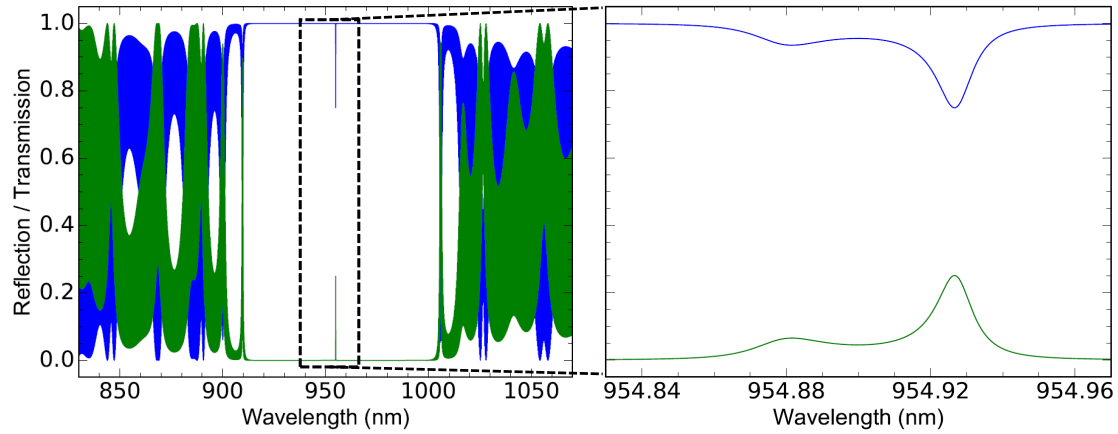

Figure 2.4: *Same as the previous figure, Fig. 2.3, for a Fabry-Pérot cavity simulated on a* 708 μm *thick substrate.*

Even though the Fabry-Pérot cavity mode is sensitive to the substrate thickness in a true micropillar cavity with transverse light confinement due to an oxide aperture, the mode waist is at the QD layer. Consequently, light reflected back from the substrate bottom surface can barely interfere with light from the QD.

For the rest of the thesis the micropillar plus substrate will be referred to as just the micropillar, and the same goes for the Fabry-Pérot.

2.4 Practical quantum information node

For the electron spin in our CQED system to function as a node it requires a long coherence time and it requires a good coupling & interaction with the photons for transferring the quantum information between nodes. For our CQED system to satisfy these two requirements it needs to be cooled down to cryogenic temperatures (increasing the electron spin coherence time) and the contacts need to be bonded such that a voltage can be applied to the device (increases the coupling and interaction with the photons).

One of the reasons cryogenic temperatures are needed is that there will be less phonons that can interact with the excitons in the QD. Quantitatively we can visualize the influence of the temperature on the electron-phonon interaction by looking at the nonradiative lifetime of the ground population of an excitonic polaron state [15]. Verzelen et al [15] show that for InAs/GaAs lens-shaped quantum dots with a radius of 10 nm the non-radiative lifetime at 300 K is 7 ps and at 77 K is 4 ns. The non-radiative lifetime is a factor of 1000 slower at 77 K than at 300 K allowing for a longer coherent electron spin. Even though the phonon's influence is smaller at lower temperature there are many other effects that decohere the electron spin at low temperature. At milli-Kelvin temperatures the main mechanism of decoherence is the coupling of the electron spin to the nuclear spins, via the hyperfine interaction[16]. The nuclear spins create a random magnetic field that leads to fluctuations in the electron spin precession and thus to decoherence. Quantitatively this happens within tens of nanoseconds.

A voltage applied to the device enables charge & energy control through the quantum-confined Stark effect [12]. Also, when a forward bias is applied it: (i) increases the absorption rate of the QD, (ii) decreases the electron tunnelling rate in the conduction band and (iii) decreases the electron-hole recombination rate in the valence band. Only an equation is given for the increase in absorption rate of the QD (i), the other two significant factors (ii) & (iii) are only briefly mentioned, because a complete picture is a study on its own. The conduction and valence band of undoped materials is flat but the doping of the materials

give the bandgap an electrostatic potential factor, which bends the conduction and valence band. As a consequence of the bending, the wavefunction of the electron and hole shift. The electron states shift to lower energies and the hole shift to higher energies. The shift reduces the electron-hole wave function overlap, thereby reducing the absorption rate between the shown electron and hole level, see Fig. 2.5.a. One can see that the absorption rate changes from Fermi's golden rule [17]:

$$W_{1\to 2} = \frac{2\pi}{\hbar}|M_{12}|^2 g(\hbar\omega) \tag{2.9}$$

Here, $g(\hbar\omega)$ is the density of states and the matrix element M_{12} describes the effect of the external perturbation caused by a light wave interacting with the electrons. The matrix element can be expanded to $M_{12} = M_{cv}M_{eh}$ with M_{cv} the conduction-valence band dipole moment and M_{eh} the electron-hole wave function overlap. The conduction-valence band dipole moment (M_{cv}) is large because it is found that GaAs and InAs have strongly allowed electric-dipole transitions between the conduction and valence bands [17]. Therefore, the important factor in determining the absorption rate is the electron-hole wave function overlap M_{eh}. It is expected that the absorption rate will be small without applying a voltage to the device, due to a small electron-hole wave function overlap, sketched in Fig. 2.5.a. The voltage induces an electric field to the z-direction of the bandgap. When a forward bias is applied the conduction and valence band move down, therefore it is expected that the overlap will become significant and thus the absorption rate will be larger, see Fig. 2.5.b. As a consequence of the larger absorption rate, the photon-QD interaction is larger.

Also, when a forward bias is applied the relative bandgap of the QD changes. This induces a wavelength shift of the QD which we can use to tune the QD in resonance with the fundamental micropillar cavity mode. Hence given us a better coupling to the light [3]. The wavelength tuning of the QD tuning is referred to as energy control. Another effect is that the forward bias applied may let the QD conduction band level fall under the Fermi level which creates a new interesting physical situation [3]. The change of the QD conduction band level is referred to as charge control.

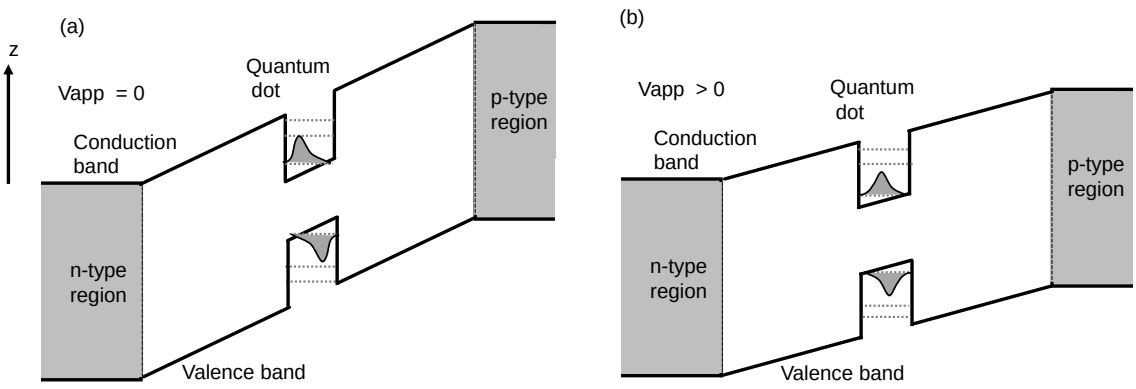

Figure 2.5: *Schematic band structure of a quantum dot (QD) embedded in a P-I-N diode. (a) no voltage is applied, but due to the electrostatic potential of the dopings the electron states shift to lower energies and the holes to higher energies, as shown by the sketch of a wave functions of the electron and hole. (b) Voltage applied, forward bias, creates an electric field in the z direction lowering the conduction and valence band due to the quantum-confined Stark effect. The forward bias also shifts the wave functions of the electron and hole. No Fermi levels are shown but the bandgap can be tuned such that the Fermi level fills up a level in the conduction band of the QD.*

Chapter 3

Theoretical coupling efficiency

In this chapter an approximation for the coupling efficiency between the 780HP single-mode fibers and the micropillar cavity is shown. The efficiency calculation is based on the overlap integral of the complex electric field of a Gaussian beam from the single-mode fibers and that from the micropillar cavity mode.

Before the coupling of the single-mode fibers to the micropillar cavity, we want to estimate the in- and outcoupling efficiencies between fibers and the micropillar cavity. For the coupling efficiency, which is a fraction of the maximum power transfer, we need the complex electric field at the fiber-micropillar interfaces at the desired wavelength. As a result that the fibers beam and micropillars photoluminescence modes are Gaussian the only important parameters for the calculation of the coupling efficiency will be the waist sizes and the position. The fiber-micropillar interface will be referred to for the input fiber as the input and for the output fiber as the output. A schematic drawing of the fiber coupling to the micropillar cavity is shown in Figure. 3.1.

For the field of the micropillar cavity we use the parameters estimated by our group [13]. It was found that the fundamental mode has a beam waist of $w_0 = 2.13 \pm 0.08$ µm at 955.1 nm. The value is found by applying a Gaussian fit to the obtained photoluminescence intensity profile of the fundamental mode. We will assume that the focus was at the exact position of the quantum dots, therefore we will rename the beam waist variable from w_0 to w_{QD}. The corresponding field is propagated to the input or output, which is achieved by employing the ABCD matrix method. For determining the waist at the input, the fundamental mode waist is propagated through the oxide aperture, the p-contact and the top DBR. For determining the waist at the output the fundamental mode waist is propagated through the n-contact, the bottom DBR and the substrate, see Fig. 3.1. To achieve this, we need the corresponding ABCD

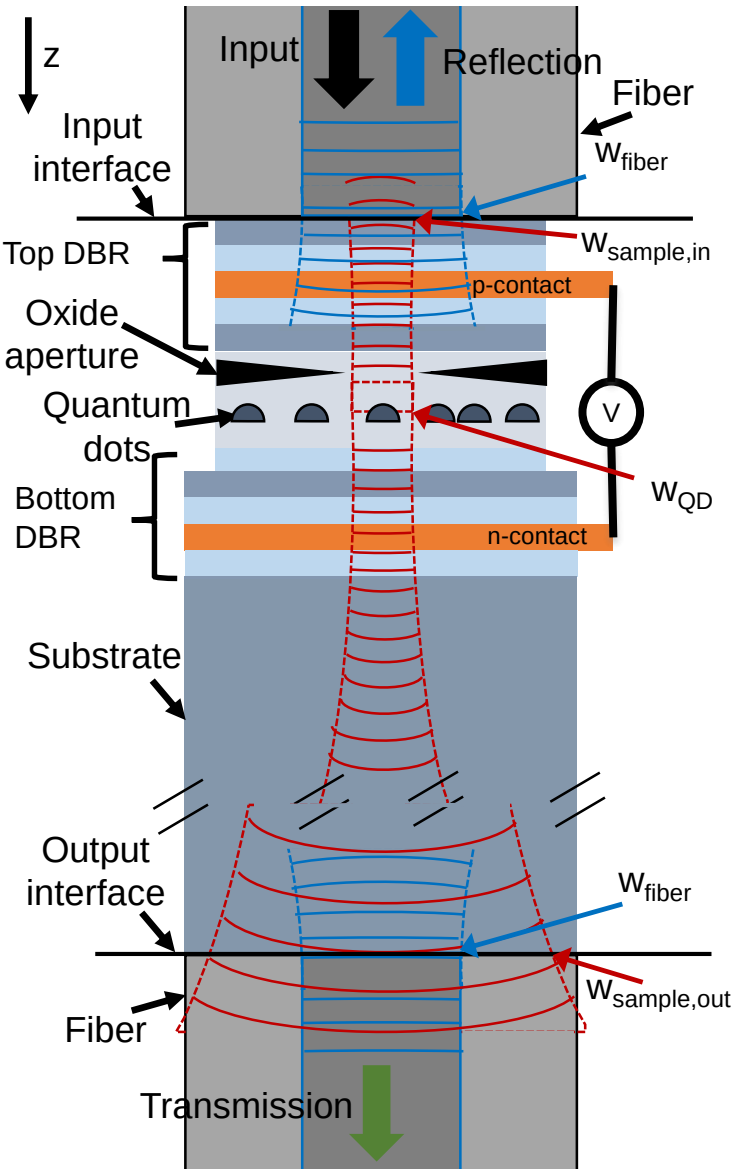

Figure 3.1: *Schematic drawing of the coupling of single-mode fibers to the micropillar cavity. It shows a sketch of the optical field from the micropillar cavity mode(red lines) with the focus at the quantum dots. The field is propagated to the input or output interface where it is coupled to the fibers mode (blue lines). The position of the waist values used for the calculation of the coupling efficiency are denoted. The substrate is broken to show the difference in length, the gallium arsenide substrate is approximately 70 times as thick as the actual micropillar.*

matrix for refraction at a flat interface and propagation through a layer [18]:

$$\text{ABCD: } \begin{pmatrix} A & B \\ C & D \end{pmatrix} \quad \text{refraction: } \begin{pmatrix} 1 & 0 \\ 0 & n_{\text{before}}/n_{\text{after}} \end{pmatrix} \qquad \text{propagation: } \begin{pmatrix} 1 & d \\ 0 & 1 \end{pmatrix} \tag{3.1}$$

Here, n_{before} and n_{after} are the refractive indices of the layers before and after refraction, respectively. d is the propagation distance in a homogeneous medium.

Usually the ABCD method is used to trace the path travelled by a light ray. Interestingly, the same matrices can be used to compute the propagation of Gaussian beams. This is achieved by employing a complex beam parameter: $q = z + iz_R$. With z the position away from the beam waist position (w_0), and z_R the Rayleigh range.

The total ABCD matrix is used to calculate the complex beam parameter at the input or output (q') from the complex beam parameter at the position of the quantum dots q:

$$q' = \frac{Aq + B}{Cq + D} \quad \text{with} \quad q = iz_R \qquad q' = z' + iz'_R \tag{3.2}$$

Here, q does not have a z part because the beam waist ($z = 0$) is situated at the position of the quantum dots. From the equation we get $z' = Re(q')$ and $z'_R = Im(q')$. With which we can calculate the waist at the input or output, $w'(z')$:

$$w'(z') = w'_0\sqrt{1 + \left(\frac{z'}{z'_R}\right)^2} \quad \text{with} \quad w'_0 = \sqrt{\frac{z'_R\lambda_0}{n\pi}} \tag{3.3}$$

In this equation, λ_0 is the wavelength in vacuum, n is the refractive index of the last medium refracted into and the Rayleigh range is given by $z'_R = \pi(w'_0)^2 n/\lambda_0$.

Plugging w_{QD} into Eq. 3.2 gives the complex beam parameter q such that q' at the input and output can be calculated from the corresponding total ABCD matrix. From the calculation we obtain for the input: $w'_{\text{in}} = 2.14 \pm 0.08$ µm and at the output $w'_{\text{out}} = 28.48 \pm 1.02$ µm. For the input waist a small difference is seen in comparison with the beam waist size w_{QD}. This can be attributed to the short length travelled by the field from the position of the quantum dots to the input, that is only approximately 4.35 µm. For the output a significant difference is seen and attributed to the approximately 700 µm thick GaAs substrate. From the w' values it is expected that the incoupling efficiency is high and outcoupling efficiency is low. From here on the $'$ is dropped such that $w'_{\text{in/out}} = w_{\text{in/out}}$.

The coupling efficiency is calculated by an overlap integral:

$$\eta = \frac{|\int E_1^* E_2 dA|^2}{\int |E_1|^2 dA \int |E_2|^2 dA} \tag{3.4}$$

Here, E_1 (E_2) is the complex electric field for the fiber (micropillar), given by Eq. 3.5. The integration spans the whole beam cross-section.

The corresponding Gaussian beam equation in cylindrical coordinates with polarisation orthogonal to the z direction and propagation in the $+z$ direction is given by:

$$E(r,z) = E_0 \frac{w_0}{w(z)} \exp\left(\frac{-r^2}{w^2(z)}\right) \exp\left(-ikz - i\frac{kr^2}{2R(z)} + i \arctan\frac{z}{z_R}\right) \tag{3.5}$$

In this equation E_0 is the electric field amplitude and phase at the origin at time 0, r is the radial distance from the center axis of the beam, k is the wave number given by $k = 2\pi/(\lambda_0/n)$ and $R(z)$ is the radius of curvature of the beam's wavefront at z given by $R(z) = z + z_R^2/z$.

The beam waist for a single-mode step-index fiber is situated at the end face, therefore at the input and output the field of the fiber becomes ($z = 0$):

$$E_{\text{fiber}}(r,0) = E_0 \exp\left(\frac{-r^2}{w_0^2}\right) \tag{3.6}$$

For the fiber we will call $w_0 = w_{\text{fiber}}$.

The fiber field in combination with the micropillar field (the Gaussian beam eq 3.5) plugged into eq 3.4 with cylindrical coordinates gives:

$$\eta = \frac{\left| \int_0^\infty r \exp\left(\frac{-r^2}{w_{\text{fiber}}^2}\right) \exp\left(\frac{-r^2}{w_{\text{in/out}}^2}\right) \exp\left(\frac{ikr^2}{2R_{(in/out)}}\right) dr \right|^2}{w_{\text{fiber}}^2 w_{\text{in/out}}^2/16} \tag{3.7}$$

Here, $w_{\text{in/out}}$ is the micropillars beam waist at the input or output and $R_{\text{in/out}}$ is the corresponding radius of curvature. From the specifications of the 780HP fiber we obtain the beam waist, $w_{\text{fiber}} = 2.5 \pm 0.25$ µm at 850 nm. The wavelength of the fundamental mode from the micropillar cavity is not at 850 nm but at 955.1 nm, therefore we calculate the fibers beam waist at the wavelength of the micropillars fundamental mode. This is achieved by usage of [19]:

$$w_{\text{fiber}} \approx a(0.65 + \frac{1.619}{V^{3/2}} + \frac{2.879}{V^6}) \tag{3.8}$$

In which a is the core radius and V the waveguide parameter, also called the V number. The V number is given by [20]:

$$V = \frac{2\pi a NA}{\lambda} \tag{3.9}$$

The 780HP core radius is 2.2 μm and the $NA = 0.13 \pm 0.03$ giving a waist of approximate $w_{\text{fiber}} = 2.95 \pm 0.25$ μm at 955.1 nm.

With the calculated values $w_{\text{fiber}} = 2.95 \pm 0.25$ μm, $w_{\text{in}} = 2.14 \pm 0.08$ μm, $w_{\text{out}} = 28.48 \pm 1.02$ μm and the corresponding values for z, $z_{\text{in}} = 4.35$ μm and $z_{\text{out}} = 704.8$ μm to calculate the corresponding radius of curvature ($R_{\text{in/out}}$), we obtain by usage of eq 3.7: $\eta_{\text{in}} = 90 \pm 7.6\%$ and $\eta_{\text{out}} = 4.1 \pm 1.1\%$. This shows that a high coupling efficiency can be expected at the input but a low coupling efficiency at the output. An important point is that the above calculated overlap integral does not take into account a transverse, longitudinal and angular misalignment which may decrease the efficiencies even more. Also not taken into account is the thin layer of epoxy between single-mode fiber and micropillar cavity, what possibly can decrease the efficiency by absorption and scattering.

To see the effects of transverse misalignment an equation is employed that neglects the phase, the phase part for the coupling efficiency is acquired from the curvature of the wavefronts ($R_{\text{in/out}}$) see Eq. 3.7, the equation only takes into account the beam waists [20]:

$$\eta = \left(\frac{2 w_{\text{fiber}} w_{\text{in/out}}}{w_{\text{fiber}}^2 + w_{\text{in/out}}^2} \right)^2 \exp\left(- \frac{2u^2}{(w_{\text{fiber}}^2 + w_{\text{in/out}}^2)} \right) \tag{3.10}$$

Here, u is the misalignment length. First we set $u = 0$ to see if the curvature of the wavefront at the input or output is a significant factor for the coupling efficiency because Eq. 3.10 does not take it into account. From Eq. 3.10 we obtain at the input: $\eta_{in} = 90 \pm 7.6\%$ and at the output $\eta_{out} = 4.2 \pm 1.1\%$. Both are very close to the values found from the overlap integral. The efficiency's found at the input is expected because the wavefronts propagated only a small part. As a consequence the wavefront is as good as flat and therefore the contribution of the wavefront curvature to the coupling efficiency is negligible. This can be seen in Eq. 3.7 by filling in a flat wavefront ($R = \text{inf}$) such that $\exp\left(\frac{ikr^2}{2R_{(in/out)}} \right) = 1$ and solving the integral, it gives the same equation as Eq. 3.10 with $u = 0$. The efficiency's found at the output is not expected to match from the two equations because a larger curvature of the wavefront is seen. As a result from the longer propagation part. Even though it is seen that the curvature of the wavefront is negligible small. Therefore, it does not contribute significantly to the outcoupling efficiency

If we fill in an offset $u = 2.2$ μm, which is half of the diameter of the 780HP core, we obtain $\eta_{in} = 44 \pm 11\%$ and $\eta_{out} = 4.2 \pm 1\%$. A significant effect on the input coupling efficiency but not on the output coupling efficiency is seen. This is due to a large decrease in the overlap of the waists of the micropillar mode and the fiber mode at the input, it can be visualized by shifting the fibers in Figure. 3.1 with u. For the output the micropillar mode beam waist is large making this small offset insignificant.

To conclude, a high incoupling efficiency is expected that is sensitive for transverse alignment and a low outcoupling efficiency is expected that is less sensitive to transverse alignment. The low outcoupling efficiency may need to be optimized later on in the process of fiber coupling, but the first tests are made with the low outcoupling efficiency.

Chapter 4

Fiber coupled devices for CQED research

In this chapter we explain the steps taken to couple fibers to a micropillar cavity. The first step for obtaining a fiber coupled micropillar is characterizing a good quality micropillar cavity. After that the process of coupling a fiber with epoxy onto the good quality micropillar cavity is explained. Also, photoluminescence measurements of a micropillar cavity are shown.

4.1 Pre-characterization of the cavity modes

Before coupling the fibers onto the micropillar, the following elements of the micropillar are checked: the cavity is polarization degenerate, if it has a QD that is close to or in the center of the cavity mode and if the QD couples qualitatively well to the cavity. A good quality cavity-QD system has a $C \gg 1$, see Eq. 2.7. Which is found by fitting the transmission dip induced by the QD [6].

For the first tests with a fiber coupled device the above is not done and the device is characterized at room temperature. At room temperature only the quality of the micropillar cavity modes will be characterized. The quality is defined by the shape, Lorentzian, and the incoupling efficiency into the fundamental mode. To make sure that we are on a micropillar cavity with the fiber we need to observe higher order modes that are split by approximately 1 nm. This is achieved by moving the fiber a bit of the center from the micropillar cavity. The reason for is that when light falls on the exact center of the micropillar cavity the higher order modes are almost invisible, but a bit of offset from the center makes the higher order modes visible.

Figure. 4.1 shows the room temperature optical set-up. We shine light from a

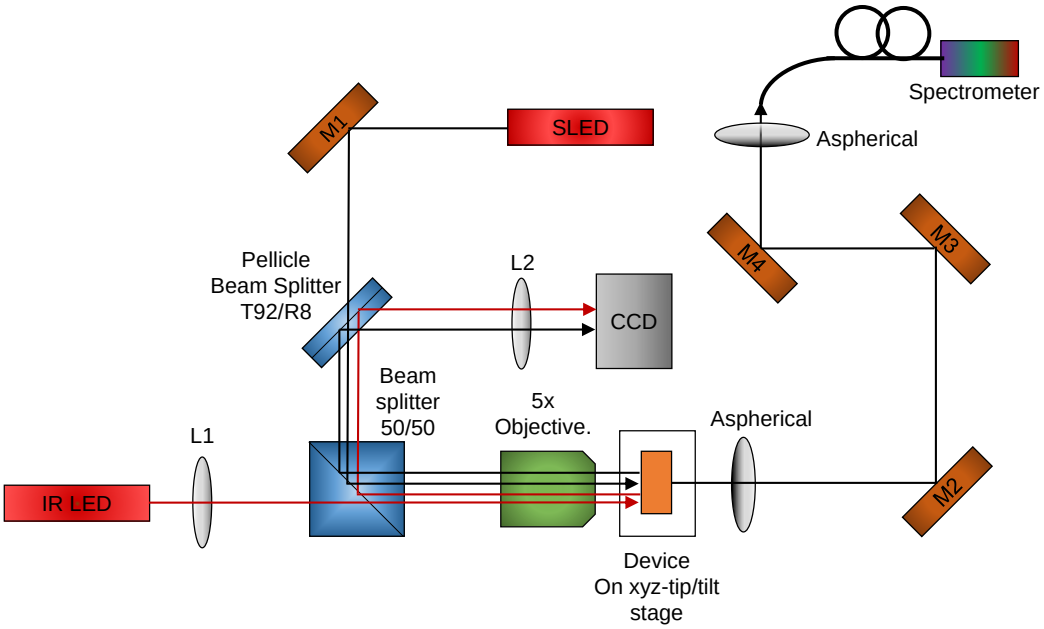

Figure 4.1: *Schematic diagram of the optical set-up used for room temperature cavity mode characterization of the device. SLED = Superluminescent diode.*

Superlum 471-HP2 superluminescent diode (SLED) onto the device and the device is illuminated with an IR LED (950 nm) which allows for the visualization of the positioning of the SLED at an arbitrary point on the device. The device's position is moved with the the xyz-tip/tilt translation stage on which it is situated. A SLED is used because it has a wide emission band, $900 - 980$ nm, and high output power, 10 mW, so that light is always coupled into the cavity mode of a Fabry-Pérot or micropillar cavity. The wavelength position of the micropillar cavity mode and Fabry-Pérot cavity mode is always a bit different, but it remains between 945 and 955 nm. The transmitted light of the cavity mode is coupled into a Horiba FHR1000 spectrograph and the spectrum is detected with an Andor DU401A BR-DD camera. The spectrograph is used with a 10 µm slit which has a corresponding spectral resolution of 0.016 nm.

Figure. 4.2 shows the transmission spectra of a good quality micropillar cavity and a Fabry-Pérot cavity close by, measured with the room temperature optical set-up. The figure also shows a SEM image with a sketch of the position of the laser for the measurements of the spectra from a Fabry-Pérot cavity and a micropillar cavity.

The Fabry-Pérot measurement shows an interference pattern especially noticeable in the right tail. The period of the peaks in the right tail can be used as

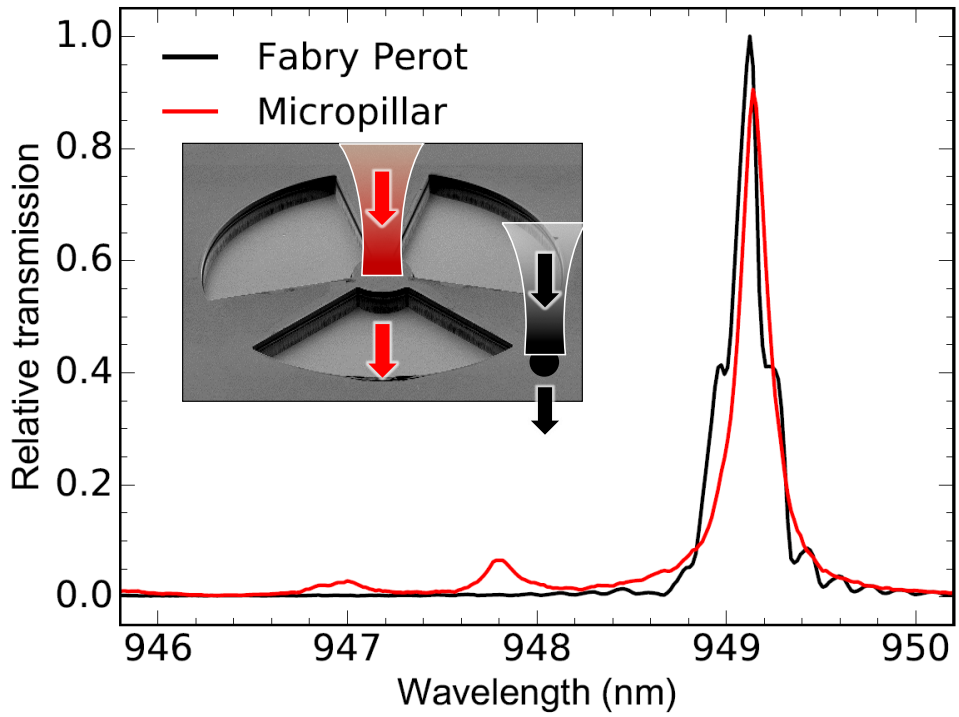

Figure 4.2: *Relative transmission spectra of the Fabry-Pérot (black line) and micropillar (red line) cavity from the room temperature set-up. Also shown is a SEM image of a micropillar area, where the two positions of the SLED light are indicated.*

the free spectral range for approximating the corresponding optical resonator length of the interference. The cavity length (l) is calculated as follow:

$$l = L/2 \quad , \quad L = \frac{\lambda^2}{n_g \Delta\lambda_{FSR}} \tag{4.1}$$

Here, L is the round trip length of the resonator, n_g is the group refractive index of the media within the resonator, λ is the vacuum wavelength of the light and $\Delta\lambda_{FSR}$ is the free spectral range of the resonator.

We fill in for the variables in Eq. 4.1, $n_g = 3.5411$, $\Delta\lambda_{FSR} = 0.17$ nm and $\lambda = 949.12$ nm as the peak value seen. The value for the group index is taken as the refractive index of GaAs, at room temperature, because most of the Fabry-Pérot is GaAs due to the thick substrate. Also, dispersion is neglected because it is negligible in this small wavelength window. With these values filled in we obtain a cavity length of $l = 748$ µm. This value may imply that the interference comes from something as thick as the substrate, probably the substrate is slightly thicker than 700 µm. The resonator may thus form between the output interface (now a substrate-air interface) and the bottom or top DBR, see Fig. 3.1.

If we compare the Fabry-Pérot spectra with the transfer matrix simulations, see Fig. 2.4, we saw that for some specific values of the substrate thickness the fundamental cavity mode splits up into two peaks. However in Fig. 4.2 we do not see the Fabry-Perot's fundamental cavity mode split into two peaks, whereas we obtain an interference pattern most noticeable in the right leg of the spectrum. As a result from this discrepancy the shown transfer matrix simulation was incomplete, the simulation does not consider an incoming gaussian beam it only considered a plane wave coming in at normal incidence.

The micropillar cavity measurement shows two higher order modes roughly split 1 nm apart ($\lambda = 947.8$ nm and $\lambda = 947$ nm). The micropillar cavity has these higher order modes due to the oxide aperture, see Section. 2.2. The micropillar cavity does not show interference, this may be attributed to the oxide aperture of the micropillar. The oxide-aperture functions as an intra-cavity lens, thence it only allows for the passage of a narrow light bundle which makes the probability of interference with the reflecting rays coming from the substrate small. The oxide aperture forces the beam waist at the position of the QDs to a size of approximately 2 μm.

After a good quality micropillar cavity mode is found the fiber coupling process can begin.

4.2 Coupling fibers to a micropillar cavity

We build an optical set-up, see Figure. 4.3, that allows us to monitor the micropillar cavity modes during the fiber coupling. If any misalignment arises during coupling we can correct for it immediately. The fiber is coupled by usage of a bare fiber terminator to the SLEDs fiber, with a coupling efficiency of around 30%. The bare fiber is held by a bare fiber holder which is mounted onto a PI xyz motorized stage. The SLED light out of the bare fiber first hits, from above, our CQED device that is mounted on a xy-rotation stage. By usage of the other elements we focus the transmitted light onto a CCD, for positioning of the fiber, and on the Horiba FHR1000 spectrograph, for monitoring the spectrum. These remaining elements are all on the optical table, except for the spectrometer. We can see through the device because the SLED spectrum goes down to 900 nm and may have a tail even further down where the device is transparent. This can be seen from the simulations, see Fig. 2.4.

The positioning of the 780HP single mode fiber onto the center of the micropillar requires high precision, because if the fiber is slightly off center we couple more into the asymmetric higher order modes and therefore the incoupling efficiency into the fundamental mode decreases, see Chapter 3. It is not efficient to couple into the higher order modes in comparison with the funda-

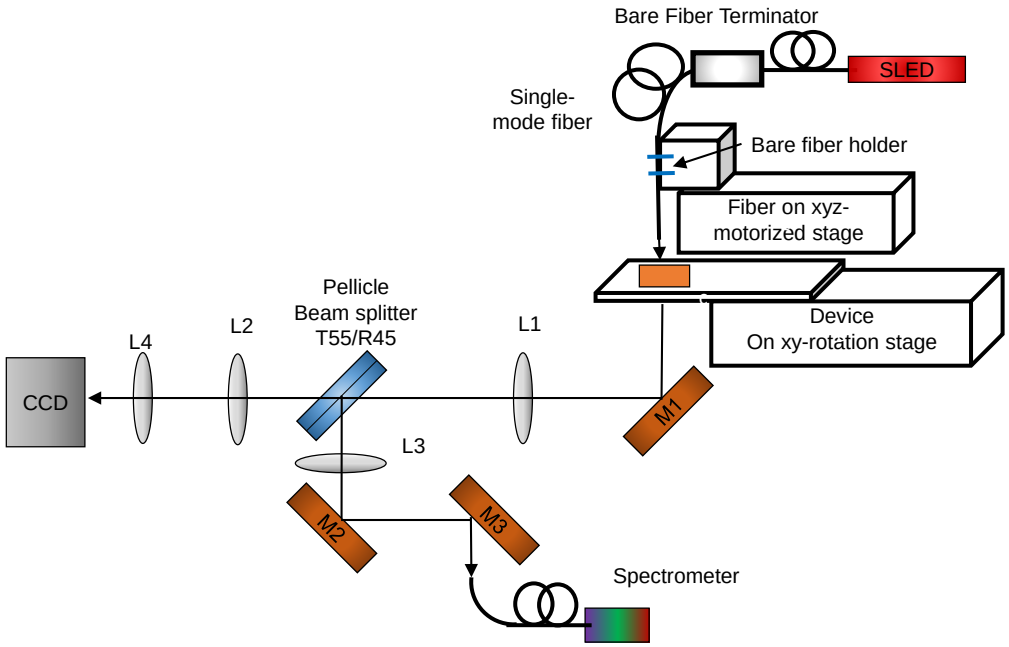

Figure 4.3: *Schematic diagram of the optical set-up used for coupling 780HP single mode fibers to a micropillar cavity. It allows for monitoring the cavity modes while coupling the fiber to the device with epoxy. The single mode fiber comes from above onto the device where the rest of the optical elements are on an optical table. SLED = Superluminescent diode.*

mental mode [3]. The 780HP fiber core is 4.4 µm in diameter and we want to position it onto a 30 µm diameter micropillar. With the precision of the motorized stage, 6.9 nm, a precise positioning of the fiber onto the center of the micropillar can be achieved.

In Figure. 4.4 the normalized transmission spectrum of the same micropillar cavity is compared from the measurement of the pre-characterization set-up and the fiber set-up. For the fiber measurement the 780HP single mode fiber is hanging 20 µm above the micropillar. The fiber measurement shows no sign of higher order modes which are split 1 nm, this can be attributed to the position of the fiber to be very close/exact at the center of the micropillar. Whereas the beam from the pre-characterization is so wide that it couples light into some of the 1 nm split higher order modes. The fiber measurement shows an interference pattern that has no periodicity from which a possible resonator length can be derived. This may be attributed to multiple factors that can create the interference. The light may interfere in the 20 µm between the fiber tip and micropillar surface, it may be one of the optical element (coating) or maybe

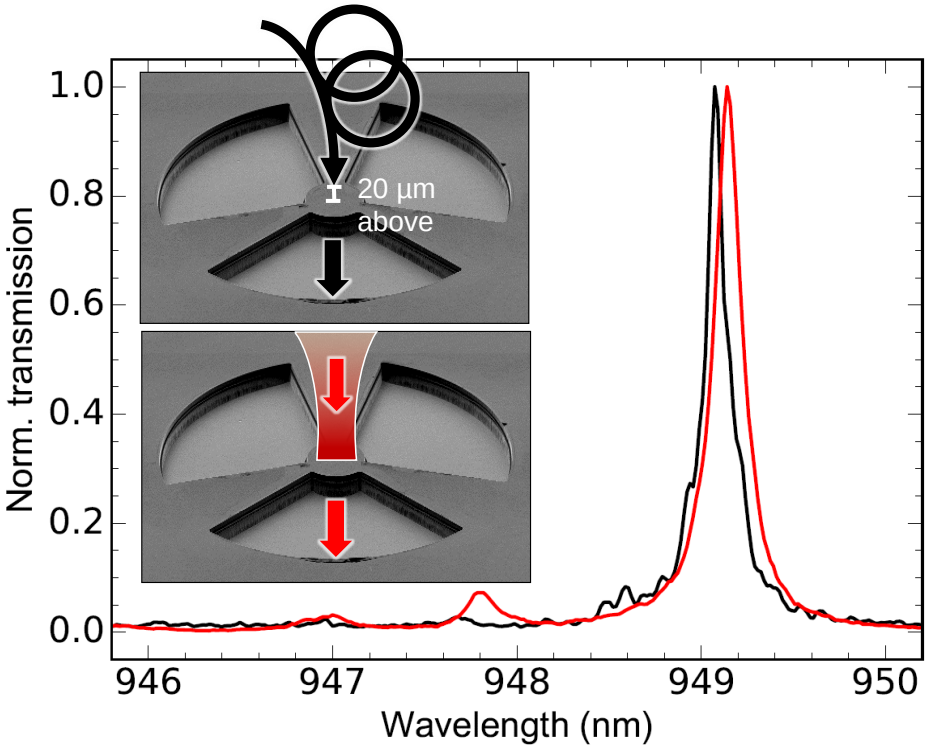

Figure 4.4: *Normalized transmission spectra of the same micropillar cavity from the pre-characterization measurement (red line) and for a 780HP single mode fiber hanging* 20 µm *above the micropillar (black line). This is also pictured by a drawing of a fiber and beam into the SEM image of a micropillar area with the corresponding line color.*

some combination of optical elements where interferences form between the elements. Also, the optical elements may induce multiple aberrations to the light that create an interference like pattern. What can also be seen from Figure. 4.4 is a wavelength shift of the fundamental mode between the two measurements. The wavelength shift is most likely due to the mounting of the device for the fiber measurement onto a copper plate with varnish. The varnish changes the strain on the device, thereby effectively changing the birefringence of the materials, which may shift the wavelength of the cavity modes. The reason that the change of the wavelength is due to strain is that it is shown by the group that strain induced by laser induced surface defects can be used to change the wavelength of the micropillar cavity modes [11].

Before coupling the fiber onto the micropillar we always checked if we are on a micropillar cavity and not for some reason on a Fabry-Pérot cavity. This is achieved by moving the fiber a little bit off the centre of the micropillar to

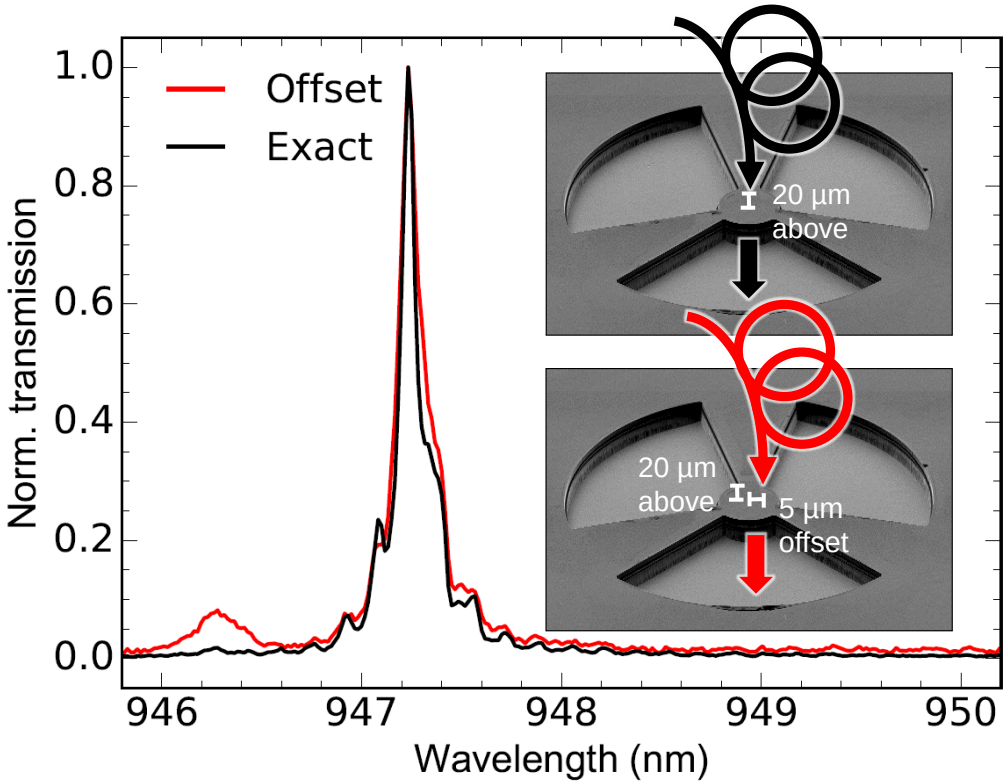

Figure 4.5: *Normalized transmission spectra of the same micropillar cavity for a 780HP single mode fiber hanging* 20 µm *above the center of the micropillar (black line) and* 5 µm *offset relative to the center (red line). This is also pictured by a drawing of the fiber into the SEM image of a micropillar area with the corresponding line color. In comparison with the plots shown before this is a different micropillar, therefore a different fundamental mode position is seen.*

couple more into the 1 nm split higher order modes. The coupling into a higher order mode split 1 nm apart is clearly visible around 946.2 nm for the red line in Figure. 4.5. In this figure the red fiber has a 5 µm offset from the centre of the micropillar and for both measurements the fiber is hanging 20 µm above the micropillar. The figure also shows that the wavelength of the peak for the fundamental mode of the measurements coincide and that the interference on the fundamental modes is situated at the same wavelengths.

As a result that we are now quite sure to be on the micropillar cavity, the fiber coupling by usage of epoxy can start. We use an UV curable epoxy, Norland Optical Adhesive 81. It has a low shrinkage, a low viscosity of 300 cps (at 25°C), a refractive index when cured around 1.56, a linear thermal expansion coefficient of 220×10^{-6} m / (m K) (at 300 K) and 95% transmission at the

wavelengths under investigation. The steps for fiber coupling with the epoxy are:

1. The fiber is stripped of its protective coating such that only the core and cladding of 125 ± 1 μm remain. This is done so that we can cleave the fiber to obtain a flat fiber end. On this flat surface a tiny droplet of epoxy, 125 μm in diameter, is put onto the fiber. The fiber comes from above on the device therefore it is likely that a radially symmetric droplet forms on the fiber tip and thus on the device.

2. The fiber with epoxy is pushed onto the device and it is cured with an ELC410 UV curing gun. During curing the micropillar's spectrum is monitored. If a misalignment of the fiber tip during curing occurs we can actively change the fiber position, if the epoxy is still fluid. The low viscosity allows for moving the fiber in the epoxy without it bending.

3. The bond is found to break under the fibers own weight when it is released from the fiber holder. Therefore, copper blocks are mounted onto the copper holder holding the device. The fiber is coupled onto the copper block with epoxy, therefore it is important that this side of the copper block has a round edge and not a sharp edge which may cut the fiber. It is found that mounting the copper block by hand, it is experimentally hard not to hit the fiber and thereby break the epoxy between the fiber and device. Therefore, a large droplet of epoxy is put onto the device after the fibers small epoxy droplet is cured. This large droplet is roughly the size of the device, 3 mm by 1.5 mm with a height of approximately 500 μm.

4. The same is done for coupling the other side with a 780HP fiber.

After the device is fiber coupled the spectra are compared when only the input is coupled with when the input and output are coupled to the same micropillar. This is shown in Figure. 4.6. The spectra shown in the figure are normalized, as a result we see that the spectra almost completely coincide. When the two measurements are compared relatively to each other it is found that the counts, when both fibers are coupled(red line), are 20 times lower than when only the input is fiber coupled(black), with the same SLED power and spectrograph integration time of 2 seconds. The lower counts for both fibers coupled is in-line with the approximation done in Chapter. 3, where the outcoupling efficiency is expected to be low, $\eta_{out} = 4.2 \pm 1.1\%$.

After the device is fiber coupled and the spectra with only the input coupled and the input and output coupled are compared the device is ready for the next step for researching cavity quantum electrodynamics. A picture of a fiber coupled device can be seen in Figure. 4.7

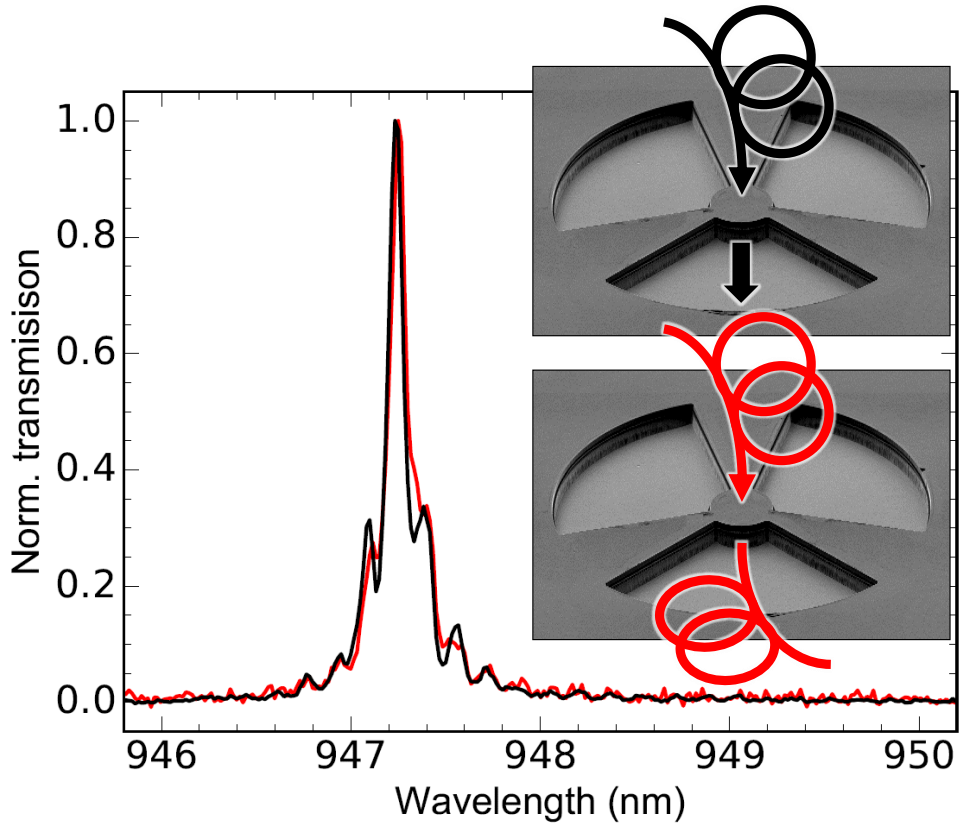

Figure 4.6: *Normalized transmission spectra of the same micropillar of a 780HP single mode fiber coupled at the input (black line) and for 780HP fibers coupled at the input and output (red line). This is also pictured by a drawing of the fibers into the SEM image of a micropillar area with the corresponding line color. It is the same micropillar as the one seen in Figure. 4.5*

4.3 Photoluminescence measurements of a micropillar cavity

We also show photoluminescence measurements of a micropillar cavity excited by a 852 nm laser (Thorlabs LP852-SF30). The photoluminescence measurements are shown in Figure. 4.8, for reflection, and in Figure. 4.9 for transmission. The transmission measurement is measured with a FG050LGA multimode fiber coupled onto the output of the micropillar, to increase the collection efficiency. It was tried with a single-mode fiber but as expected from the approximation of the outcoupling efficiency, $\eta_{out} = 4.2 \pm 1.1\%$, no photoluminescence signal in transmission was detected with a 780HP single-mode fiber.

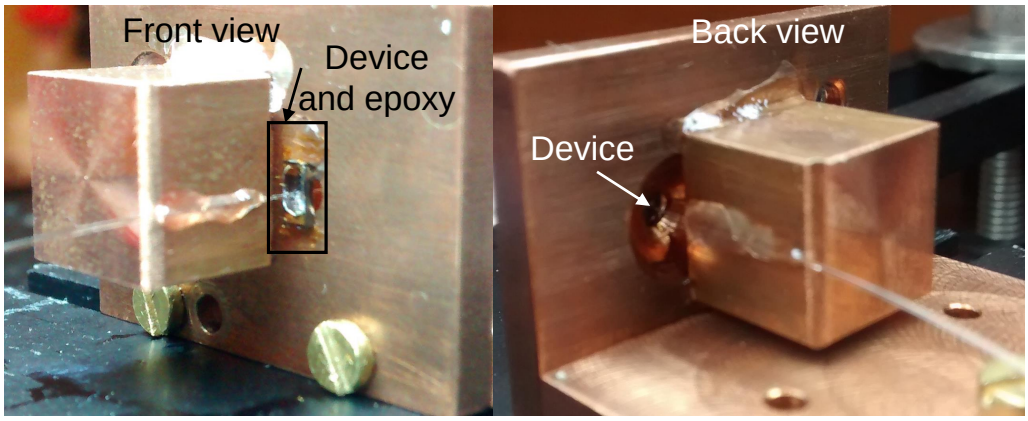

Figure 4.7: *Picture of the device fiber coupled at the input (front view) and output (back view). A lot of epoxy can be seen on the device that covers its total surface and even goes a bit onto the copper holder for the device, in the front view picture. Both the input and output fiber are glued onto a copper block.*

The photoluminescence seen is most likely from the electrons of GaAs and the wetting layer that are pumped above the bandgap which move towards the QD where the electrons recombine and emit photons into the cavity modes (for GaAs the bandgap is: 870 nm at 300 K [21] and the bandgap of the wetting layer is also around this value [3]).

Both spectra show higher order micropillar cavity modes that are split roughly 0.4 nm apart. The splitting value is less then the earlier stated 1 nm, this may be attributed to the fact that it is a different micropillar cavity. As a consequence the fundamental waist size might be different which changes the splitting of the higher order modes [13]. The spectra also still show interference which is due to the device, between fiber and device and the current optical set-up. See the previous section. The transmission spectrum shows the peaks a bit shifted in wavelength in comparison with the reflection spectrum. The wavelength shift is most likely due to a strain change in the device because of the coupling with epoxy of the two fibers.

Photoluminescence measurements in reflection and transmission are viable but the amount of light collected into the single-mode (reflection) and multi-mode (transmission) fiber is low. Therefore, long integration times are needed. As a consequence photoluminescence can not be used during the active monitoring of the epoxy process. Most significantly because no quick position change of the fiber can be made without the user immediately seeing the effect of the change in the spectrum. Therefore, the SLED is preferred over the 852 nm laser.

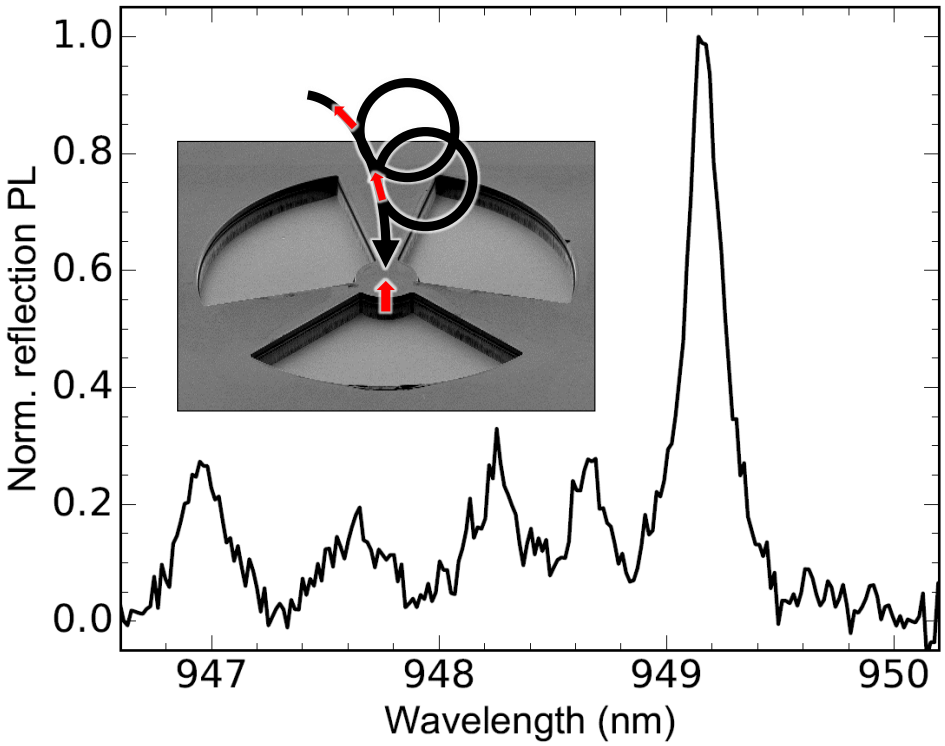

Figure 4.8: *Normalized reflection photoluminescence spectrum of a micropillar cavity with a 780HP fiber in contact with the surface of the micropillar. It is not attached with epoxy, the fiber is softly pushed onto the device. The photoluminescence is excited with a 852 nm laser.*

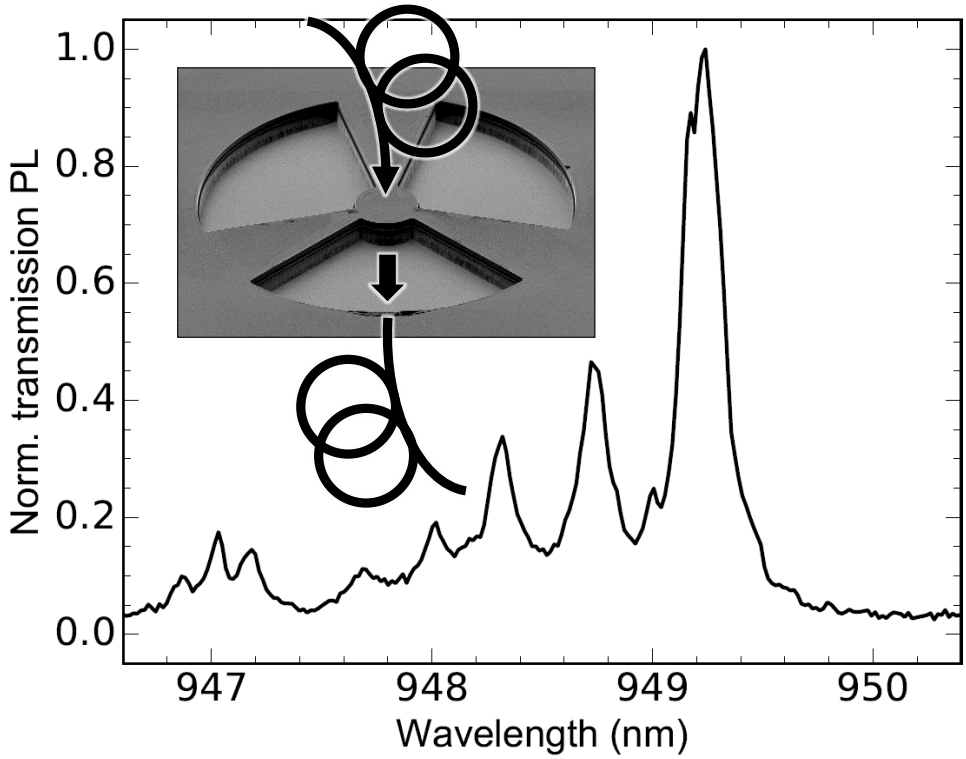

Figure 4.9: *Normalized transmission photoluminescence spectrum of a micropillar cavity with a 780HP fiber coupled to the input and a multi-mode FG050LGA coupled to the output. The photoluminescence is excited with a 852 nm laser. Note this is the same micropillar as for the reflection photoluminescence measurement, Fig. 4.8*

Chapter 5

Cooling a fiber coupled device down to cryogenic temperatures

In this chapter measurements of the first tests with cooling down a fiber coupled device are shown and discussed. The measurements shown are from two cool down cycles. After the first cool down cycle the micropillar cavity modes disappeared, but during the second cool down cavity modes remained visible until 3.5 *K.*

5.1 First cool down cycle measurements

We show and discuss the measurements of cooling down our device that has 780HP single-mode fibers coupled to the input and output of a micropillar cavity. As discussed in Section. 2.4 cooling down the device is needed for preserving electronic coherence in the QDs. We do not expect to see typical signatures of QDs because the contacts are not bonded for these first tests. As a consequence the photon-QD interaction is expected to be low and the QDs wavelength are not tunable into the cavity mode, see Section. 2.4. A typical signature of QDs is that it creates a small narrow dip in the transmission of the cavity mode [4].

The fiber coupled device is put into a modified Entropy pulse-tube cryostat. Two optical fibers can enter the cryostat, each through a Swagelock tube fitting containing a teflon tube. The fibers coupled to the device are each fusion spliced onto a 780HP bare fiber that has on one end an FC/APC connector. The FC/APC connector side with half of the fibers length remains on the outside of the cryostat the rest of the fibers length, including the spliced parts, are in the cryostat. The input fiber is connected to the superluminescent diode and the output fiber is connected to a Horiba 550 Triax spectrograph. The spectrum is

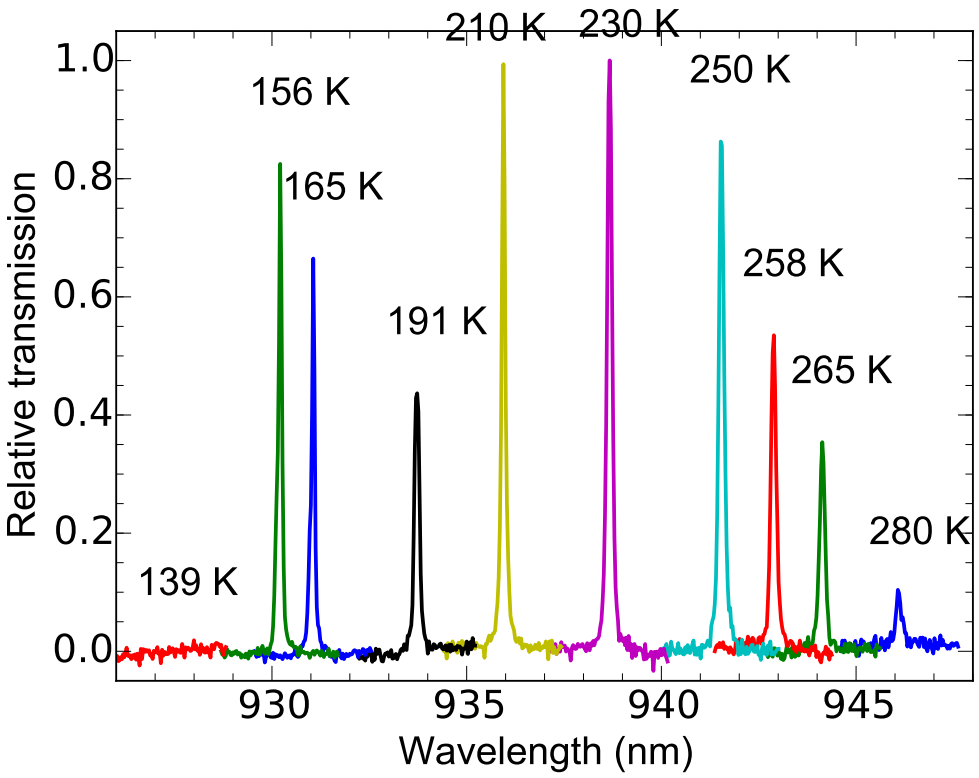

Figure 5.1: *Relative transmission spectra of the fundamental mode of a micropillar cavity that is coupled at the input and output with 780HP single-mode fibers. Shown at different temperatures. The temperature values that correspond to the fundamental mode seen are denoted above it.*

detected with an Andor DU401A BR-DD. The spectrograph is used with a 10 μm slit and has a corresponding spectral resolution of 0.03 nm.

Figure. 5.1 shows the first cool down measurements. In this figure the relative transmission spectrum of the fundamental mode of a fiber coupled micropillar cavity at different temperatures is shown. The temperature sensor is mounted close, 3 cm apart, to the copper plate on which the device is mounted. The cooling rate of the cryostat is 0.0425 K/min. During the whole cooling down process a wavelength shift of the fundamental mode is seen. The wavelength shift is partly due to a change in the effective cavity length. How the cavity length influences the wavelength of the fundamental mode is shown by the equation of the transmission(T) for an optical cavity . From this equation a resonance condition arises for the transmission [22]:

$$T = \frac{1}{1 + (4\mathcal{F}^2/\pi^2)\sin^2(\phi/2)} \quad \text{with} \quad \phi = \frac{4\pi n L_{\text{cav}}}{\lambda} \tag{5.1}$$

Here, $\mathcal{F}$ is the finesse of the cavity, L_{cav} is the cavity length, λ is the wavelength in vacuum and n is the refractive index of the cavity. The transmission is equal to unity whenever $\phi = 2\pi m$ with m an integer number. This occurs when $L_{\text{cav}} = m\lambda/2n$, referred to as the resonance condition. During cooldown a change in the wavelength of the fundamental mode is seen. The wavelength change in combination with a tiny change in the refractive index of GaAs with decreasing temperature [23] changes the effective cavity length.

Also seen in Figure. 5.1 is an increase in counts from 280 K up to 210 K. At 191 K the counts are lower but the counts do increase again during the cool down cycle. Then at 139 K the signal is gone and it remains gone up to the cryostat's minimum temperature of 3.5 K. The change in counts is most likely because of the large droplet of epoxy put onto the device, which enables the placement of the copper blocks against the fiber, see Section. 4.2. The epoxy used has a high linear thermal expansion coefficient 220×10^{-6} m / (m K), which in comparison with copper (16.6×10^{-6} m / (m K)), GaAs (6×10^{-6} m / (m K) and fused silica (0.55×10^{-6} m / (m K)) is at least a factor of 10 larger. All values for the thermal expansion coefficient are shown for 300 K. During cool down the coefficients become smaller but it is expected that the epoxy coefficient remains high in comparison with the other coefficients. The contraction of the large droplet of epoxy may move the position of the single mode fibers, thereby changing the coupling into the fibers. The movement of the fiber may especially happen when the large droplet is not symmetric. We expect the large droplet to be asymmetric because of the large size. In the end one or both of the fibers are probably completely misaligned and therefore no signal is seen any more. The contraction of the epoxy may also induce strain on the device. The consequence of the strain on the device is a possible wavelength shift of the fundamental mode, see discussion about Figure. 4.4. In worst case scenario it is even possible that the strain broke part of the device.

5.2 Second cool down cycle measurements

The signal during the first cool down was lost from 139 K onwards so the cryostat was warmed up. During the warming up from 3.5 K the spectrum was monitored and suddenly a signal arose around 133 K. We stopped the warming up procedure and cooled down again to 3.5 K while monitoring the spectrum. This is shown in Figure. 5.2.

The 133 K measurement shows what looks like a fundamental mode, the peak around 934.5 nm and possibly two higher order modes around 933.6 nm and 932.2 nm. This indicates that the light may originate from the micropillar cavity. The fundamental mode is monitored during cool down to 33 K, but a

peak is starting to arise in its left tail. This gives an indication that again the contraction of the epoxy is moving one or both of the fibers. Most likely the input fiber is now moved a bit off center because it looks as if more light is coupled into a higher order mode that is only split 0.2 nm. The measurement at 30 K shows three very low peaks that do not resemble any of the spectra seen at 33, 75 and 133 K. This spectrum is seen to remain until the end of the cool down process towards 3.5 K. The three peaks are most likely due to strain induced by the epoxy, see Section. 5.1. Important to note is that the three peaks are not(!) QDs because they are to wide 0.1 nm. The fact that we do not see QDs is expected because the contacts are not bonded for these tests.

The signal obtained at 3.5 K is found to be polarization sensitive. This was tested by connecting the input fiber to a 780HP fiber that is mounted in a Thorlabs manual fiber polarization controller. The polarization controller uses stress-induced birefringence, this is achieved by wrapping the fiber around three spools to create three independent wave plates which when rotating a plate change the polarization of the light by twisting the fiber [24, 25]. The wave plates are two $\lambda/4$ plates and one $\lambda/2$ plate. Shown in Figure. 5.3 when the splitting between the two different polarized inputs is the highest, approximately 0.4 nm. Therefore, it is expected that for the maximum splitting a $\lambda/2$ retardance is applied.

The signal seen is light coming from the micropillar cavity because it has three peaks that are split 0.8 and 1.4 nm apart and it is polarization sensitive, implying that we do not have a polarization degenerate micropillar cavity.

From these first tests with cooling down a fiber coupled device arose the problem that the transmission signal is completely changed or gone when cooling down to 3.5 K. Both effects originate most likely from the large epoxy droplet used which has a large linear thermal expansion coefficient. As a consequence, the contraction of the epoxy probably shifts the fibers off the micropillar, strain tune the device and maybe even break the device. Nevertheless we have shown full input-output fiber based polarization control of a micropillar cavity at 3.5 K which is essential for letting the device function in a photon polarization based quantum network.

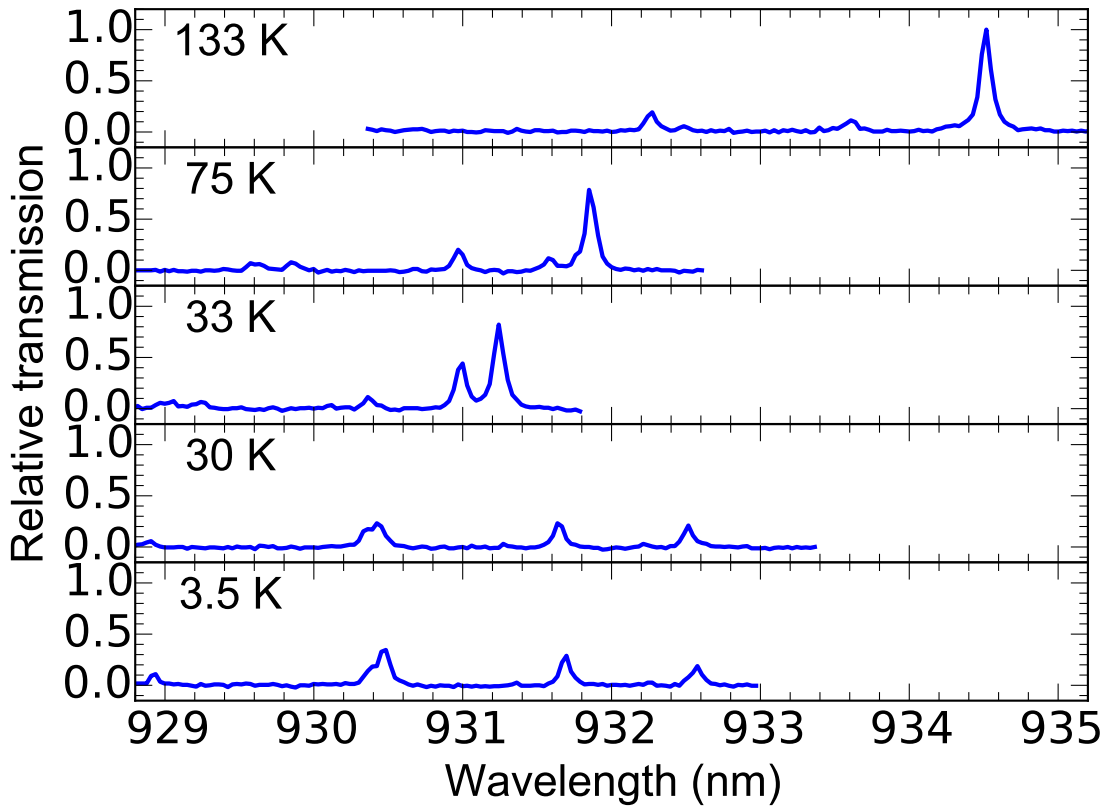

Figure 5.2: *Relative transmission spectra of a 780HP fiber coupled micropillar cavity during cooldown. It is the same fiber coupled device as seen in Figure. 5.1 of which the transmission signal was lost during cool down. The device was warmed up and the signal returned at* 133 *K which was then cooled down again to* 3.5 *K, these measurements are shown here. The temperature values corresponding to the spectra are indicated.*

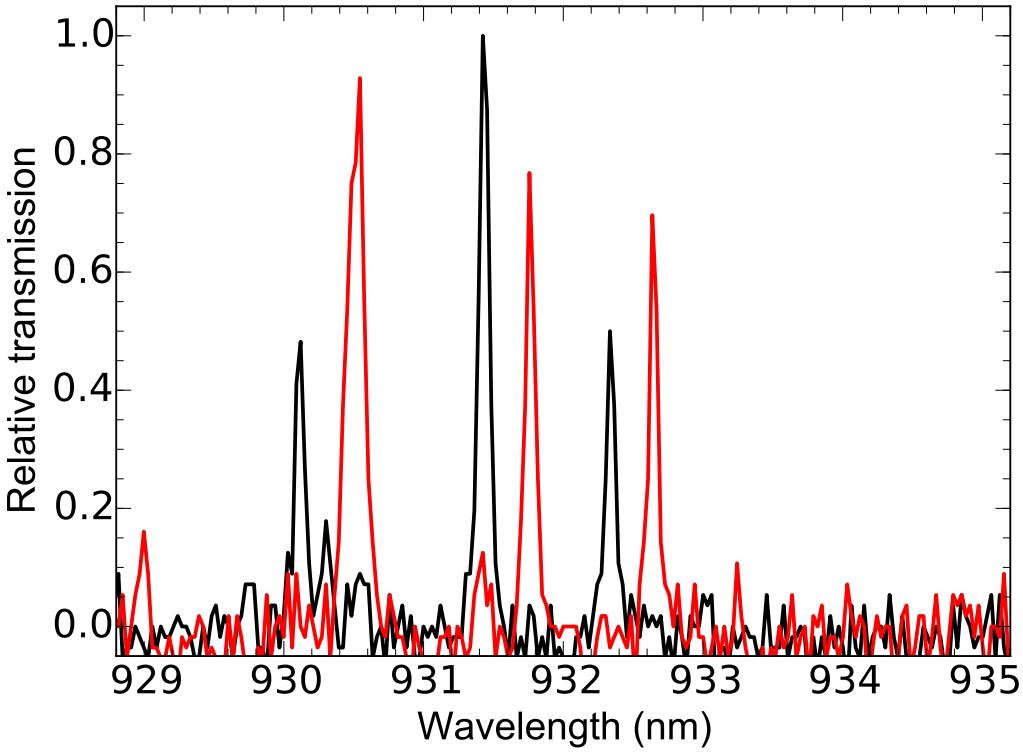

Figure 5.3: *Relative transmission signal of the micropillar cavity at 3.5 K, seen in Fig. 5.2. The spectra are made when the polarization of the incoming light is different. The black and red line are orthogonal ($\lambda/2$) to each other in polarization.*

Chapter 6

Conclusion & Outlook

We have shown how to achieve a single-mode fiber coupled micropillar cavity that allows us to research cavity quantum electrodynamics. From the first tests of cooling down the fiber coupled micropillar cavity, experimental challenges arose. These likely originated from the contraction of a large asymmetric epoxy droplet with a high linear thermal expansion coefficient, used for coupling the fibers onto the micropillar cavity.

The challenge of a too large NOA81 epoxy droplet may be solved by using less epoxy, thereby only coupling the fibers with an epoxy droplet on the tip of the fiber. The small epoxy droplet came with the experimental challenge that during mounting of the copper block by hand the block will hit the fiber and break the bond. Nonetheless we can solve the experimental challenge. For example: place the copper blocks mechanically onto to the holder against the fibers or the copper blocks are already attached onto the holder of the device before the fibers are coupled. Another solution may be exploring other adhesives with the same optical specifics but with a lower thermal expansion coefficient, for example: AMS technologies AT4291A which comes at a cost of having a high viscosity. The high viscosity may give problems with making small position adjustment during curing, it may bend the fiber. A different adhesive may also be used in combination with NOA81, for example: NOA81 used for the fiber tip and a low shrinkage adhesive around the tip which therefore does not need the same specifics as NOA81. An example of such an adhesive is Stycast.

The fiber coupling can also be improved by increasing the out coupling efficiency. No measurements are made of the exact value of the in and out coupling efficiency but it is found from experiments that the out coupling efficiency is low, because the power of the SLED and the integration time of the spectrograph needed to be raised. For example the spectra of Fig. 4.6 has the signal a factor of 20 times lower when the output is fiber coupled in comparison to the

light gathered in free space, with the same power of the SLED and the same integration time of the spectrograph The low output signal of a fiber coupled device is in-line with a theoretical approximation for where the out coupling efficiency is calculated to be low, $\eta_{out} = 4.2 \pm 1.1\%$. A possible solution to this problem may be removing the thick substrate from the device. Another solution may be inserting a graded index lens between the device and fiber such that the light from the quantum dots is focused onto the front face of the fiber.

Even though there are still some challenges that need to be solved we have shown full input-output fiber based polarization control of a micropillar cavity at 3.5 K, which makes the outlook exciting. A fiber coupled cavity quantum electrodynamics device may pave the way for a more scalable approach for building a large-scale quantum network. Also, it opens up the possibility of creating a fiber based non-classical light source.

References

[1] G. H. Oettinger, *European commission will launch a 1 billion euro quantum technologies flagship*, 2016.

[2] S. Ritter, C. Nölleke, C. Hahn, A. Reiserer, A. Neuzner, M. Uphoff, M. Mücke, E. Figueroa, J. Bochmann, and G. Rempe, *An elementary quantum network of single atoms in optical cavities*, Nature **484**, 195 (2012).

[3] J. Gudat et al., *Cavity quantum electrodynamics with quantum dots in microcavities*, Department of Quantum Optics and Quantum Information, Leiden Institute of Physics (LION), Faculty of Science, 2012.

[4] M. P. Bakker et al., *Cavity quantum electrodynamics with quantum dots in microcavities*, PhD thesis, Leiden Institute of Physics (LION), Quantum Optics, Faculty of Science, Leiden Univesity, 2015.

[5] T. Heindel, C. Schneider, M. Lermer, S. Kwon, T. Braun, S. Reitzenstein, S. Höfling, M. Kamp, and A. Forchel, *Electrically driven quantum dot-micropillar single photon source with 34% overall efficiency*, Applied Physics Letters **96**, 011107 (2010).

[6] H. Snijders, J. Frey, J. Norman, M. Bakker, A. Gossard, J. Bowers, M. van Exter, D. Bouwmeester, and W. Löffler, *Purification of a single photon nonlinearity*, arXiv preprint arXiv:1604.00479 (2016).

[7] D. Ding et al., *Cavity quantum electrodynamics with rare-earth ions in solids*, PhD thesis, Institute of Physics, Faculty of Science, Leiden University, 2015.

[8] F. Haupt, S. S. Oemrawsingh, S. M. Thon, H. Kim, D. Kleckner, D. Ding, D. J. Suntrup III, P. M. Petroff, and D. Bouwmeester, *Fiber-connectorized micropillar cavities*, Applied Physics Letters **97**, 131113 (2010).

[9] A. Reiserer and G. Rempe, *Cavity-based quantum networks with single atoms and optical photons*, Reviews of Modern Physics **87**, 1379 (2015).

[10] E. T. Jaynes and F. W. Cummings, *Comparison of quantum and semiclassical radiation theories with application to the beam maser*, Proceedings of the IEEE **51**, 89 (1963).

[11] C. Bonato, D. Ding, J. Gudat, S. Thon, H. Kim, P. M. Petroff, M. P. van Exter, and D. Bouwmeester, *Tuning micropillar cavity birefringence by laser induced surface defects*, Applied Physics Letters **95**, 251104 (2009).

[12] D. Miller, D. Chemla, T. Damen, A. Gossard, W. Wiegmann, T. Wood, and C. Burrus, *Electric field dependence of optical absorption near the band gap of quantum-well structures*, Physical Review B **32**, 1043 (1985).

[13] C. Bonato, J. Gudat, K. de Vries, S. M. Thon, H. Kim, P. M. Petroff, M. P. van Exter, and D. Bouwmeester, *Optical modes in oxide-apertured micropillar cavities*, Optics letters **37**, 4678 (2012).

[14] S. J. Byrnes, *Multilayer optical calculations*, arXiv preprint arXiv:1603.02720 (2016).

[15] O. Verzelen, R. Ferreira, and G. Bastard, *Excitonic polarons in semiconductor quantum dots*, Physical review letters **88**, 146803 (2002).

[16] J. Fischer, *Spin decoherence of electrons and holes in semiconductor quantum dots*, PhD thesis, University_of_Basel, 2010.

[17] M. Fox, *Optical properties of solids*, volume 3, Oxford university press, 2010.

[18] B. E. Saleh and M. C. Teich, *Fundamentals of photonics*, volume 22, Wiley New York, 1991.

[19] D. Marcuse, *Loss Analysis of Single-Mode Fiber Splices*, Bell System Technical Journal **56**, 703 (1977).

[20] A. Ghatak and K. Thyagarajan, *An introduction to fiber optics*, Cambridge university press, 1998.

[21] M. El Allali et al., *Experimental determination of the GaAs and Ga 1- x Al x As band-gap energy dependence on temperature and aluminum mole fraction in the direct band-gap region*, Physical Review B **48**, 4398 (1993).

[22] M. Fox, *Quantum optics: an introduction*, volume 15, OUP Oxford, 2006.

[23] J. McCaulley, V. Donnelly, M. Vernon, and I. Taha, *Temperature dependence of the near-infrared refractive index of silicon, gallium arsenide, and indium phosphide*, Physical Review B **49**, 7408 (1994).

[24] R. Ulrich and A. Simon, *Polarization optics of twisted single-mode fibers*, Applied optics **18**, 2241 (1979).

[25] R. Ulrich, S. Rashleigh, and W. Eickhoff, *Bending-induced birefringence in single-mode fibers*, Optics letters **5**, 273 (1980).